Instabilities within Rotating mode-2 Internal Waves

David Deepwell[1], Marek Stastna[1], and Aaron Coutino[1]

[1]Department of Applied Mathematics, University of Waterloo, Waterloo, Canada

Correspondence to: David Deepwell (ddeepwel@uwaterloo.ca)

Abstract. We present high resolution, three dimensional simulations of rotation modified mode-2 internal solitary waves at various rotation rates and Schmidt numbers. Rotation is seen to change the internal solitary-like waves observed in the absence of rotation into a leading Kelvin wave followed by Poincaré waves. Mass and energy is found to be advected towards the right-most side wall (for Northern hemisphere rotation) which led to Kelvin-Helmholtz instabilities within the leading Kelvin wave that form above and below the pycnocline. These instabilities are localized within a region near the side wall and intensify in vigour with increasing rotation rate. Secondary Kelvin waves form further behind the wave from either resonance with radiating Poincaré waves or the remnants of the K-H instability. The first of these mechanisms is in accord with published work on mode-1 Kelvin waves. Both types of secondary Kelvin waves form on the same side of the channel as the leading Kelvin wave. Comparisons of equivalent cases with different Schmidt numbers indicate that while low Schmidt number results in the correct general characteristics of the modified ISWs, it does not correctly predict the trailing Poincaré wave field or the intensity and duration of the K-H instabilities.

1 Introduction

Over recent decades nonlinear internal solitary waves (ISWs) have been the subject of continuing research due, in part, to their common presence in coastal waters (Shroyer et al. (2010) and Lamb (2004)) and estuaries (Bourgault and Kelley (2003)), and an expanding set of applications, such as plankton and krill transport (Scotti and Pineda (2004)) or cross-shelf transport (Hosegood and van Haren (2004)). Of particular interest are the effects that rotation has on these waves, since they have been observed to have lifetimes such that this effect is non-negligible (Farmer et al. (2009)). At observation sites such as Knight inset (Klymak and Gregg (2001)) and within the St. Lawrence river (Mertz and Gratton (2013)), side walls may also impact the propagation of these waves. Indeed, classical linear wave theory for rotation modified waves demonstrates that the presence of side walls allows a different type of wave to be created, namely a Kelvin wave.

The dominant insights on Kelvin waves in a channel geometry come from the experimental work of Maxworthy (1983), and Renouard et al. (1987). These authors performed lab-scale experiments in which mode-2 (Maxworthy (1983)) and mode-1 (Renouard et al. (1987)) Kelvin waves were generated in a rectangular domain. They found that though the wave amplitude increased at the channel wall with increasing rotation rate, the phase speed and shape were comparable to waves of similar amplitude in the presence of no rotation. The authors also described how the wave amplitude decayed exponentially away from the wall, how the wave front was curved backwards, and how the waves decayed as they propagated away from the

generation site due to the generation of inertial waves. In Sánchez-Garrido and Vlasenko (2009) the authors discussed numerical simulations constructed to approximately model the evolution of mode-1 waves in the Strait of Gibraltar. When the latitude was increased to 60 degrees, the authors found clear evidence of a secondary tail of Poincaré waves which trailed the leading Kelvin wave and extracted energy from this wave. The authors also found clear evidence of Mach stems. As this study provides

5   a direct comparison work to our own, its results will be discussed at various points in the following.

In the simpler case of a rotating fluid adjusting without the presence of side walls, it has been observed that if dispersive effects are accounted for, a leading solitary wave is created which then breaks down into a nonlinear wave packet as it propagates (Coutino and Stastna (2017)). Additionally, a geostrophic state is created at the site of the initial condition which oscillates at a near inertial frequency and radiates waves. Previous work based on hydrostatic equations (Kuo and Polvani (1997)) had

10   suggested that the nonlinear waves created would steepen and eventually break, however, when dispersive effects are accounted for, breaking does not occur and a nonlinear wave packet is generated instead. This effect has been observed in lab scale experiments using the Coriolis Rotating Platform in Grenoble (Grimshaw et al. (2013)). To account for these effects the authors used model equations based on the rotation modified Korteweg-de Vries (KdV) or Ostrovsky equation, which gave qualitatively similar results to the observations. However, these equations do not account for the full nonlinearity which accounts for the

15   differences to Coutino and Stastna (2017) where the full Euler equations were used.

The work by Fedorov and Melville (1995) showed that if dispersive effects are neglected (when nonlinearity is large) the Kelvin waves will break. Specifically, the authors found that rotation delays the onset of breaking by 60%. When the breaking occurs, it simultaneously forms across the zone of uniform phase that is normal to the boundary. The increase in nonlinearity is seen to create a dipole structure in the cross-shelf velocities. On a similar note, (Kuo and Polvani (1997)) note that time to

20   breaking depends on both the rotation rate and the steepness of the initial conditions (see their Figure 18 for details). However, it is unclear how a more realistic model with short wave dispersion would modify these results.

There have been a number of studies on Kelvin waves from a model equation approach. Grimshaw (1985) derived a rotation-modified Korteweg-de Vries (rKdV) equation whose transverse structure is that of a linear Kelvin wave. The author also showed that when rotation is weak, (the internal Rossby radius is much larger than the wavelength of the wave) the evolution is

25   described by the rotation-modified Kadomstev-Petviashvili (rKP) equation. This was followed up by Katsis and Akylas (1987) who performed a numerical simulation of these equations and found that the wave amplitude varied exponentially across the channel and the wave front was curved backwards in agreement with the results seen in Maxworthy (1983) and Renouard et al. (1987).

ISWs within a cylindrical geometry have also been investigated by Ulloa et al. (2014) and Ulloa et al. (2015) using an

30   immersed boundary numerical method. The authors found that the rotation rate affected the nonlinear steepening which further caused a degeneration of the fundamental Kelvin wave into a solitary-type wave packet. When the Kelvin wave amplitude was large enough, localized turbulent patches were produced by Kelvin wave breaking. However, we estimate that a single turbulent patch has a vertical extent of about 40 cm and contains approximately 25 points. Since the features within this turbulent patch are highly chaotic, it is doubtful that the small-scale structure contained within this region were sufficiently resolved.

While results on non-rotating mode-2 ISWs, especially with regards to their mass transport capabilities (Deepwell and Stastna (2016); Salloum et al. (2012); Brandt and Shipley (2014); Terez and Knio (1998)), are readily available, however the case of mode-2 ISWs in a rotating reference frame has only been investigated experimentally by Maxworthy (1983). We extend that research with a focus on the breaking of the rotation modified ISW (or Kelvin wave, depending on one's choice of terminology) at the focusing boundary.

The remainder of the paper is structured as follows: the set up of the numerical experiments and numerical methods are outlined first, with the results that follow structured to identify fundamental differences between rotating and non-rotating evolution, characterize the three-dimensional structure of near wall overturning, and point out the importance of keeping a realistic Schmidt number than $Sc = 1$, which has been consistently used in past literature.

1.1 Configuration of Numerical Experiments

We have run a series of direct numerical simulations in a setup similar to that of Maxworthy (1983). These experiments employed a gravity intrusion in a rectangular domain in a rotating reference frame to generate mode-2 waves. On experimental scales, both the gravity intrusion and the subsequent set of rank-ordered mode-2 internal solitary-like waves are modified by rotation.

We form the gravity intrusion by releasing a large perturbation into a quiescent, quasi-two-layer background stratification (Figure 1). Algebraically, the density field has the form,

$$\rho(x,z) = \rho_0 - \frac{\Delta\rho}{4}\left[\tanh\left(\frac{z-z_0-\eta(x)}{h}\right) + \tanh\left(\frac{z-z_0+\eta(x)}{h}\right)\right],$$

where

$$\eta(x) = \frac{H_m}{2}\exp\left[-\left(\frac{x}{L_m}\right)^p\right],$$

describes the perturbation in which H_m, L_m, and p set the height, width, and transition length, respectively. This stratification leads to a single hyperbolic tangent profile for $x \gg L_m$ and a double hyperbolic tangent profile with an intermediate density layer for $x \ll L_m$. The pycnocline is centred on the mid-depth, while the rest of the stratification parameters are listed in table 1. For comparison, the domain size is $6.4\text{ m} \times 0.4\text{ m} \times 0.3\text{ m}$.

Table 1. Stratification parameters.

H_m (m)	L_m (m)	p	$\Delta\rho/\rho_0$	z_0	h
0.1	0.3	8	0.02	0.15	0.02

We have completed a suite of numerical simulations at various rotation rates and Schmidt numbers. The rotation rate has been specified using the Coriolis parameter, f, which is defined in the usual way as twice the rotation rate. We define our maximum Coriolis parameter as $f_0 = 0.105\text{ s}^{-1}$ which is comparable to the literature (Grimshaw et al. (2013)) and in particular to values achievable in the Coriolis Rotating Platform.
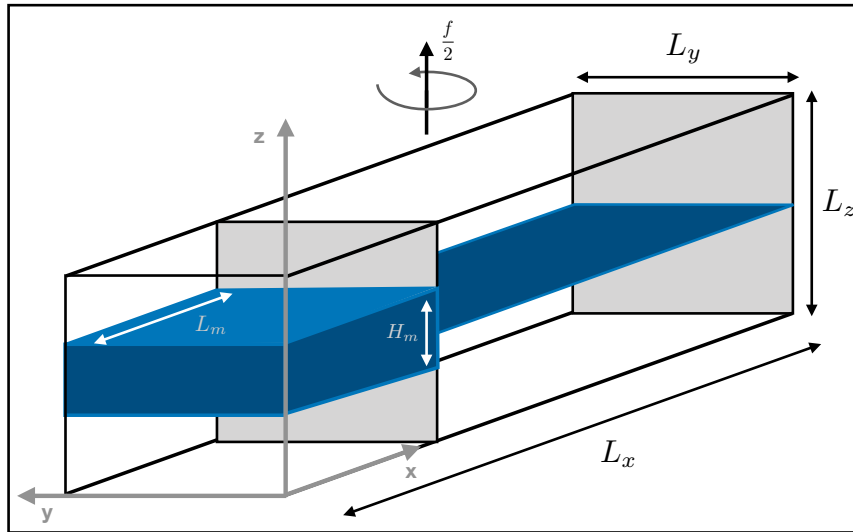
Figure 1. Schematic of the numerical domain. The blue region corresponds to $\rho = \rho_0$ with heavier fluid below and lighter fluid above.

We characterize the parameters of the leading wave in regard to their size at the $y = 0$ m wall. In particular, the wave speed, c_w, and amplitude, a_w, will be parametrized at this boundary because it is where they reach their maximal values due to the focusing of mass and energy by rotation. The amplitude is defined as the maximum upstream displacement of the $\rho(z_0 \pm h)$ isopyncals just prior to the formation of instabilities. The internal Rossby radius of deformation is thus defined as $L_c = c_w/f$, the Rossby number as $\text{Ro} = c_w/fL_m$, the Reynolds number as $\text{Re} = c_w L_m/\nu$, and the Schmidt number as $\text{Sc} = \nu/\kappa$. The kinematic viscosity was $\nu = 2 \times 10^{-6}$ m^2/s for all cases, whereas the mass diffusivity, κ, varied. The parameters and characteristic values for each simulation are presented in table 2. The velocity is scaled by the linear, non-rotating, long wave speed, $c_0 = \frac{1}{2} (gh\Delta\rho/\rho_0)^{1/2}$ (Benjamin (1967)). The average rate of change of the amplitude is given by $a' = -\frac{T}{h}\frac{da_w}{dt}$, where $T = L_m/c_0$ is the characteristic time scale.

We briefly contrast our set-up to that of Sánchez-Garrido and Vlasenko (2009). The primary difference is the scale to be modelled. While we seek to model laboratory scale motions, and hence resolve both tank scale and small scale motions, in Sánchez-Garrido and Vlasenko (2009) the authors seek to model field scale motions. Hence their ratio of depth to span-wise extent is much smaller than ours. Moreover they model dissipation through an eddy viscosity, while we attempt to carry out a Direct Numerical Simulation (DNS). Nevertheless, the ratio of their Rossby radius to span-wise extent is roughly 0.6, hence similar to some of our experiments. Thus many of the large scale motions in the two sets of simulations can be expected to be similar. In particular, Figure 2 of Sánchez-Garrido and Vlasenko (2009) makes for a useful comparison to some of our findings.

Table 2. Case parameters and characterizations.

Case	Sc	f/f_0	c_w/c_0	a_w/h	a'	Re	Ro	L_c (m)
10_0	10	0	1.48	1.47	1.83	6960	∞	∞
10_1/16	10	1/16	1.49	1.45	2.47	7010	23.74	7.12
10_1/4	10	1/4	1.48	1.49	6.02	6960	5.90	1.77
10_1/2	10	1/2	1.46	1.53	6.40	6870	2.91	0.87
10_1	10	1	1.47	1.61	6.76	6900	1.46	0.44
4_0	4	0	1.48	1.46	2.03	6930	∞	∞
4_1/2	4	1/2	1.45	1.53	5.96	6820	2.89	0.87
4_1	4	1	1.46	1.61	6.62	6870	1.45	0.44
1_0	1	0	1.44	1.41	2.88	6770	∞	∞
1_1/2	1	1/2	1.41	1.50	4.97	6640	2.81	0.84
1_1	1	1	1.44	1.61	6.32	6780	1.43	0.43

1.2 Numerical Methods

The governing equations used within our numerical model are the stratified Navier-Stokes equations with the f-plane and Boussinesq approximations (Kundu et al. (2012)),

$$\frac{D\boldsymbol{u}}{Dt} + (-fv, fu, 0) = -\frac{1}{\rho_0}\nabla p + \frac{\rho}{\rho_0}\boldsymbol{g} + \nu\nabla^2\boldsymbol{u},$$

$$\nabla \cdot \boldsymbol{u} = 0,$$

$$\frac{D\rho}{Dt} = \kappa\nabla^2\rho,$$

where each variable has their usual meaning. The Navier-Stokes equations are presented in dimensional form, while the remainder of this article will use the following non-dimensionalizations,

$$\widetilde{x} = x/L_m, \quad \widetilde{y} = y/L_y, \quad \widetilde{z} = z/L_z,$$

$$\widetilde{t} = t/T,$$

$$\widetilde{\rho} = (\rho - \rho_0)/\rho_0,$$

where the later is called the density anomaly. Scaling time by the rotation rate is inapplicable because the flow is predominantly a Kelvin wave. Rather, time has been scaled by $T = L_m/c_0$ since the propagation speed of a Kelvin wave is equivalent to the gravity wave speed in the absence of rotation.

Numerical simulations were completed using the Spectral Parallel Incompressible Navier-Stokes Solver (SPINS) (Subich et al. (2013)). SPINS is a psuedo-spectral method uniquely capable of solving the given problem to a high degree of accuracy

in the given geometry. The third-order Adams-Bashforth method with an adaptive time step was used to evolve the flow. Free slip boundary conditions were specified on all walls.

The size of the channel and the grid resolution are listed in Table 3. The stated resolution was sufficient for all but two simulations: case 10_1 and case 4_1. These both had the resolutions in the x and z dimensions doubled to have the total number

5 of points be $4096 \times 256 \times 512$. Grid convergence studies were conducted for these cases because they were the most energetic with the largest and most energetic density overturns. Good agreement was found for the cases with the stated resolution and those with half the resolution. In general, the higher resolutions have been used in this article because of their higher accuracy, though bulk characteristics of the flow computed at the lower resolution remain accurate.

Table 3. Tank dimensions and numerical resolution.

L_x (m)	L_y (m)	L_z (m)	N_x	N_y	N_z	Δx (mm)	Δy (mm)	Δz (mm)
6.4	0.4	0.3	2048	256	256	3.1	1.6	1.2

2   Results: Influence of rotation

10 We begin by looking at how the ISW is affected by rotation through the Coriolis force. We have chosen the rotation to match that of the Northern Hemisphere which causes objects to be deflected towards the right of their trajectory. In the context of our experiment this leads to span-wise variation in the developing ISW. Maxworthy (1983) found that the wave front became curved as a result of variation of the celerity on wave amplitude. At $\widetilde{y} = 0$ (which we will call the focusing wall) the amplitude and celerity were both larger than at other y values.

15 We investigate the location of the ISW crests using the scaled, vertically integrated kinetic energy,

$$\xi(x,y,t) = \frac{\int_0^{L_z} \text{KE} \, dz}{\max_{x,y,t} \int_0^{L_z} \text{KE} \, dz} \tag{1}$$

where the kinetic energy is defined in the usual way, $\text{KE} = \frac{1}{2}\rho_0 \left(u^2 + v^2 + w^2\right)$, and the maximum is over space and time.

The time evolution of ξ displays the bending of the leading internal Kelvin wave and the developing Poincaré waves for case 10_1 (figure 2). Early on (figure 2a), the energy is mostly within the leading wave since insufficient time has passed for

20 radiation to occur. However, at this early time, the wave, which began as a plane wave across the channel, has clearly been affected by the rotation as evidenced by energy being focused towards $\widetilde{y} = 0$. This focusing also resulted in the curvature of the leading Kelvin wave front, a phenomenon which remains evident for the remainder of the simulation.

As time progresses, Poincaré waves form behind the Kelvin wave, as previously described by Sánchez-Garrido and Vlasenko (2009). The Poincaré waves reflect multiple times off both the $\widetilde{y} = 1$ and $\widetilde{y} = 0$ walls. At $\widetilde{t} = 10.4$ ($t = 100$ s) the ratio of total

25 KE on the $\widetilde{y} = 1$ wall to the $\widetilde{y} = 0$ is approximately 0.11 indicating that location of primary activity will be near the focusing wall. The shear also reaches its maximum in this location, enabling the onset of dynamic instabilities.
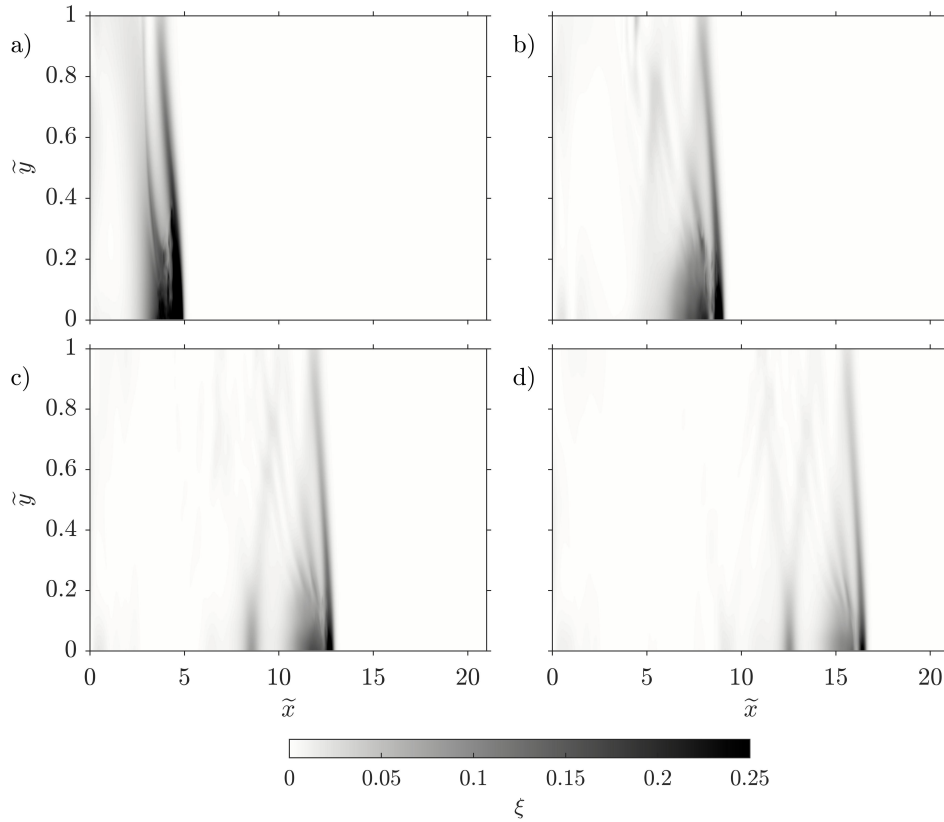
Figure 2. The time evolution of the scaled, vertically integrated kinetic energy, ξ, for case 10_1 at $t =$ a) $\widetilde{t} = 2.6$ ($t = 25$ s) b) $\widetilde{t} = 5.2$ ($t = 50$ s) c) $\widetilde{t} = 7.8$ ($t = 75$ s) d) $\widetilde{t} = 10.4$ ($t = 100$ s). Colour axis is saturated at early times to show the wave at later intervals.

The presence of the Kelvin and Poincaré waves in this context is quite common and is dependent on the rotation rate (figure 3). An increasing rotation rate leads to an increase in the angle that the leading wave makes with the normal of the boundary. The Poincaré waves behave similarly as the rotation rate is varied, however they also have the added complication of reflection and non-linear interaction between waves. When rotation is absent (figure 3a), Poincaré waves are unable to form; instead,

5 a simple train of three planar ISWs of decreasing amplitude and energy are formed. Overall, the energy within the Poincaré waves is considerably smaller than the energy in the leading wave, at least over the duration of our numerical experiments.

It needs to be mentioned that the presence of side walls removes the possibility of a span-wise invariant geostrophic state forming in the collapse region since the presence of walls enforces that flow is in the along tank direction. This means that the release of mass and energy into the ISWs is greater than when no side wall is present. The detailed dynamics of the near field

10 are interesting, but beyond the present manuscript.

A secondary boundary trapped wave also forms in the rotation modified cases (figure 3b-d). The generation mechanism for this wave is fundamentally distinct from the formation of trailing ISWs in the non-rotating case. In discussing this difference,
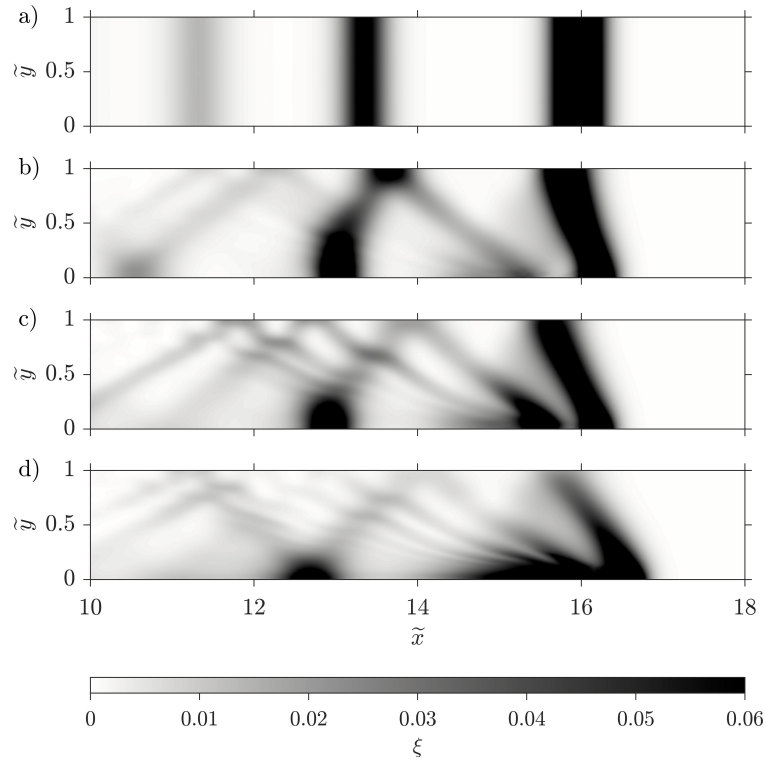
Figure 3. Scaled, vertically integrated kinetic energy, ξ, at $\widetilde{t} = 10.4$ ($t = 100$ s) for case with $f/f_0 =$ a) 0 b) 1/4 c) 1/2 d) 1. The scaling is by the maximum over the $f = f_0$ case and the colour axis is saturated to emphasize the Poincaré waves emanating from the focusing region and their reflection off the $\widetilde{y} = 1$ wall. Though in non-dimensional form, the axes have correct dimensional scaling.

ISW will be used to describe the non-rotating waves only, while Kelvin and Poincaré waves will naturally be understood to relate to the rotation modified waves. To see how this secondary Kelvin wave is formed, figure 4 compares the span-wise average ξ of the non-rotating case (case 10_0, in red) to that of the full ξ for case 10_1 (black pseudocolour). At the early time, $\widetilde{t} = 4.7$ ($t = 45$ s), there is a single leading Kelvin wave and a few radiating Poincaré waves which are just beginning to reflect off the $\widetilde{y} = 1$ wall. The trailing ISWs of the non-rotating case are completely unrelated to the energy distribution of the rotating case. This is clearly evident in figure 4 b) and c) where the second trailing ISW is located where very little energy exists in the rotating case. The third ISW is near where the second Kelvin wave is forming, but this happens to be a coincidence of the choice of the presented time. Later, at $\widetilde{t} = 10.4$ ($t = 100$ s) (figure 3) the third ISW is well behind the second Kelvin wave.

More importantly, at high rotation rates the second Kelvin wave is clearly formed by a resonance with the Poincaré waves at the focused wall, which is directly contrary to how the trailing ISWs form without rotation (they are the excess mass that isn't trapped by the leading wave). This description appears to be valid for rotation rates greater than $f/f_0 = 1/4$, since rates slower than this show that the trailing Kelvin wave matches the generation of a trailing ISW in the non-rotating case with additional perturbations due to Poincaré waves.
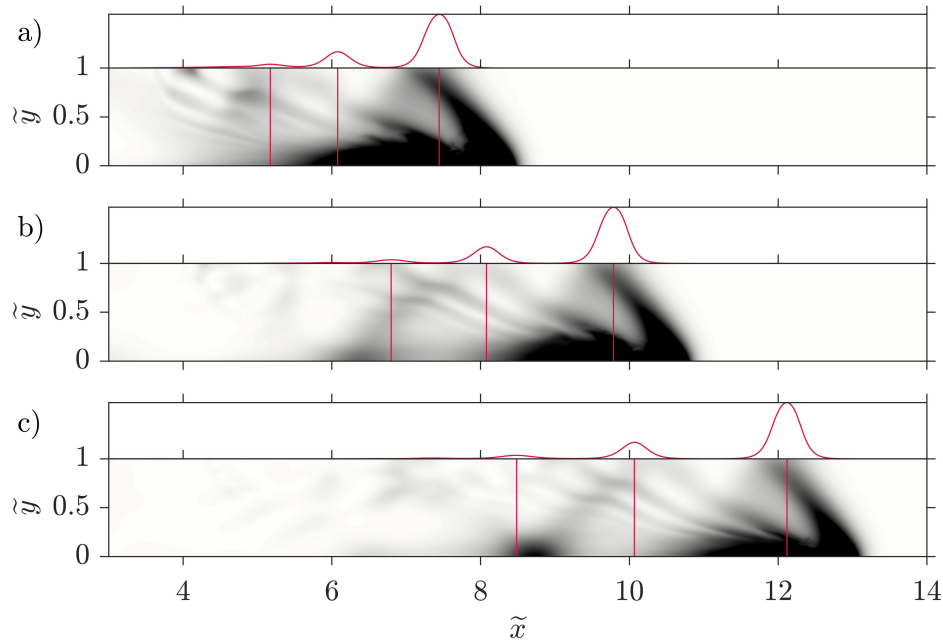
Figure 4. Scaled, vertically integrated kinetic energy, ξ, for case 10_1 at $t =$ a) $\widetilde{t} = 4.7$ ($t = 45$ s) b) $\widetilde{t} = 6.3$ ($t = 60$ s) c) $\widetilde{t} = 7.8$ ($t = 75$ s).
Scaling and colour axis is identical to figure 2. The red plots are the span-wise average ξ profiles for the non-rotating case (Case 10_0), with
corresponding maxima locations (vertical lines).

As described by Sánchez-Garrido and Vlasenko (2009) the Poincaré waves will continue to remove energy from the leading
Kelvin wave, which is then deposited in this secondary Kelvin wave. This deposition primarily occurs on the focusing wall,
as opposed to equal deposition on both sides of the channel, because of the broken symmetry caused by the collapse of
intermediate fluid on one end of the channel. This means that there is more residual kinetic energy at $\widetilde{y} = 0$ (compared to

5   $\widetilde{y} = 1$), and that the time for the Poincaré wave to resonantly interact with the Kelvin wave is greater at $\widetilde{y} = 0$ since both are
traveling in the same direction. Once the secondary Kelvin wave is fully developed, this resonance can be considered analogous
to a Mach stem in that the energy builds up on the boundary enough that the reflection no longer occurs at the boundary, and
moves instead some distance away from the wall.

As energy is drained from the leading Kelvin wave and deposited into the secondary wave, the secondary wave will eventu-

10   ally become more energetic than the first resulting in an eventual overtaking. Our simulations do not show this feature since our
channel is not long enough and we are focused on the shorter time scales associated with the energetics of the leading Kelvin
wave. See Sánchez-Garrido and Vlasenko (2009) for a description of overtaking.

The differentiation of whether a wave is a Kelvin wave or a Poincaré wave is made difficult because of the non-linearity
associated with the large amplitude of these waves. The classical linear theory presented by Kelvin describes a Kelvin wave

15   as one which has no span-wise velocity, and where the wave crest does not curve in the span-wise direction. A simple check
shows that the leading and radiating waves have significant span-wise velocities which would indicate that they are not Kelvin
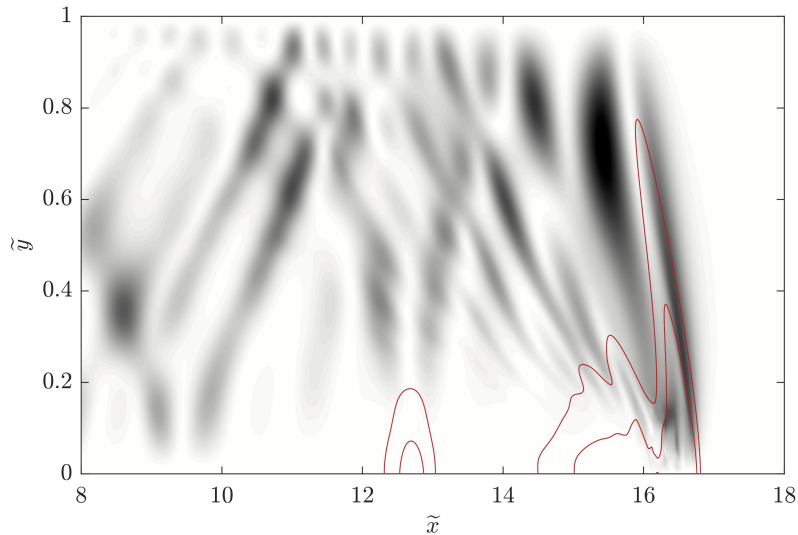
Figure 5. Vertically integrated v^2 at $\widetilde{t} = 10.4$ ($t = 100$ s) for case 10_1. Red contours are level curves of the vertically integrated KE.

waves (in the classical sense). However, we choose to label the radiating waves as Poincaré waves and the leading wave as a Kelvin wave because both fit all other descriptions of the particular wave type.

We just saw that the radiating Poincaré waves resonate to form a secondary Kelvin wave. Since this secondary wave is separated from the chaotic leading wave, it could possibly fit better in the description of a classical Kelvin wave. Figure 5

5   presents a test for this by plotting the vertically integrated span-wise squared velocity (in dark) and contours of the total vertically integrated KE (in red). The secondary wave (at $\widetilde{x} \approx 12.5$) does indeed show no span-wise velocity or wave crest curvature, and thus our description of it as a Kelvin wave is valid. We also notice that the region directly trailing the wave also has little to no span-wise velocity. Looking back at figure 3b and c it becomes clear that there are Kelvin waves directly trailing the leading wave at weaker rotation rates (the highest rotation rate requires more time to settle into this description).

10   This Kelvin wave is distinct from the previously described secondary wave. In this case they are formed out of the remains of the excess focused mass along $\widetilde{y} = 0$. To distinguish this Kelvin wave from the leading wave, we call it the Kelvin wave tail.

The dynamics seen thus far are fundamentally different than in the case without the side walls. As described in Coutino and Stastna (2017), without the walls the Poincaré waves steepen and eventually breakdown into a non-linear wave packet as dispersive effects take over. The addition of side walls appears to slow the large-scale breakdown of the leading wave. Rather,

15   this energy is moved towards the side wall, and is then radiated leeward into trailing Poincaré waves at a slower pace.

The advection of kinetic energy within the Kelvin and Poincaré waves is key to understanding how the distribution of this energy is influenced by the side wall. The span-wise flux of KE (figure 6) reveals some interesting features. Of primary interest is the leading Kelvin wave which has both positive and negative span-wise flux of KE. Close to the wall (figure 6c), the front of the wave has advection away from the wall, which then becomes a stronger, more localized, return of kinetic energy flux
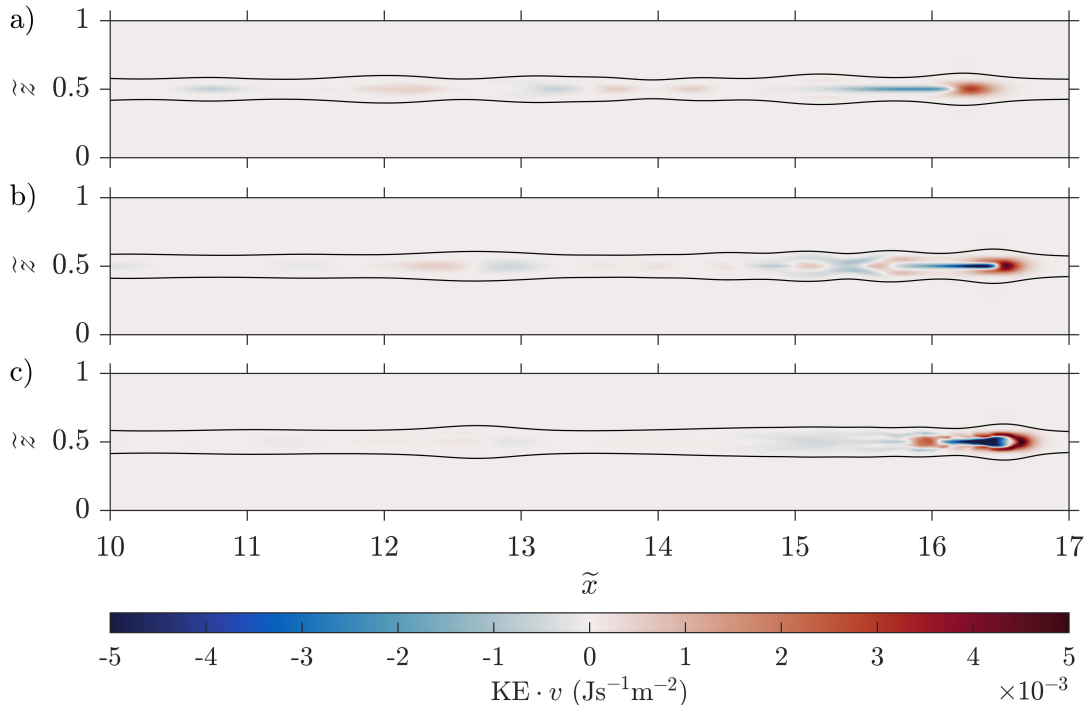
Figure 6. Span-wise kinetic energy flux density for case 10_1 at $\widetilde{t} = 10.4$ ($t = 100$ s) and $\widetilde{y} =$ a) 1/2 b) 1/4 c) 1/8.

towards the wall within the downstream portion of the leading wave. Further from the side-wall (figure 6a), the KE flux is weaker by nearly an order of magnitude and the structure has changed so that the leading wave contains more positive flux.

The secondary Kelvin wave (near $\widetilde{x} = 12.75$ m) has much weaker KE flux even though the waves are of comparable amplitude. The leading wave still contains residual energy from the K-H instabilities while the secondary wave receives energy

5 from upstream. To within 3%, the same KE flux is advected towards and away from the focusing wall in this secondary Kelvin wave.

For comparison purposes, we have completed the same simulation in two dimensions while allowing transverse flow to be coupled to horizontal motion through the Coriolis force (i.e. a two-and-a-half dimensional model). Since there exists no side wall, the radiated ISWs are smaller because much of the energy remains within the geostrophic state. Regardless of the waves

10 being smaller and thus traveling slower, the KE flux in the leading wave of the 2D case (not shown) is different from that of the 3D case with sidewalls, especially near the wall. Further from the side walls, the two become more similar yet remain distinct in the magnitudes and distributions of the KE flux.

The span-wise variation in the KE flux along the mid-depth ($\widetilde{z} = 0.5$ m) further describes the KE flux away and towards the focusing wall. Figure 7 displays both the magnitude of the flux (colour) and direction (streamlines) in a reference frame

15 moving with the wave. The strongest KE flux is directed towards the wall in the aft of the Kelvin wave. We hypothesize that
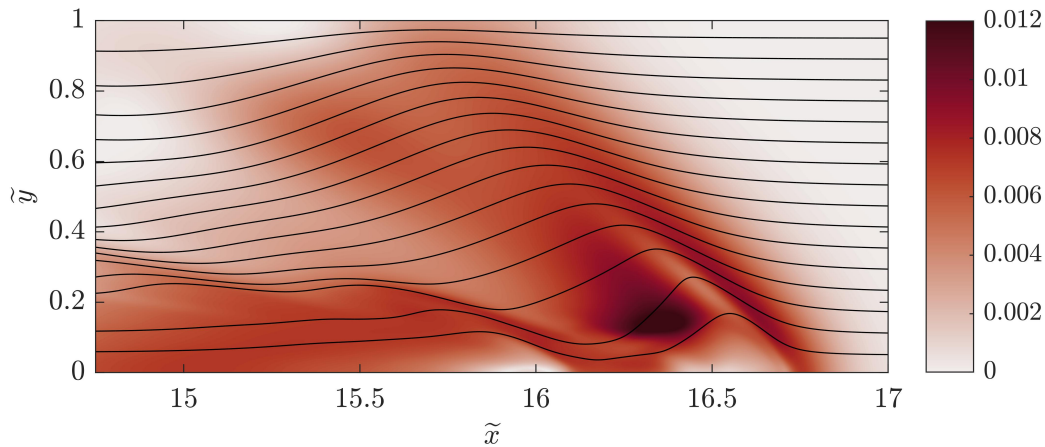
Figure 7. Horizontal kinetic energy flux density for case 10_1 at $\widetilde{t} = 10.4$ ($t = 100$ s) and $\widetilde{z} = 0.5$. Streamlines show direction of KE flux in reference frame moving with the leading wave (i.e. flow is right to left). Colour axis shows magnitude of KE flux.

this KE flux is the cause of wave breaking in the Kelvin wave (the details of which we present in the next section). The kinetic energy near the wall then leaves the Kelvin wave and travels along the wall until forming the Kelvin wave tail some time later.

3   Results: Details of wave breaking

Now that the description of the global wave field has been presented, we move onto the localized behaviour of the leading
5   Kelvin wave at the focusing wall. As described by Maxworthy (1983), the dominant instability takes the form of a pair of Kelvin-Helmholtz (K-H) billows at the crests of the leading Kelvin wave at the upper and lower extrema of the wave (figure 8a), and confined to within approximately ten centimetres (a quarter of the channel width) of the focusing wall (figure 8b-d).

For all cases, the Kelvin-Helmholtz billows simultaneously form as pairs with a vortex above and below the pycnocline. Furthermore, except during the early energetic K-H formation, these billows remain synchronous even during the process of
10   being broken down. For a while it appeared as though case 10_1 made a transition from simultaneous K-H formation to an oscillatory one. However, this transition disappeared when the resolution was increased to properly resolve this case. Whether the vortices form simultaneously or not, they are visually analogous to a von Karman vortex street. We note that there is no quantitative correspondence since the object is not a solid, there are no boundary layers, and the rotation rate is an additional parameter which affects the form of the vortex street.

15   At the wave crest, the wave has the expected exponential decay (figure 8d). Further behind, a description that is purely in the $\widetilde{x} - \widetilde{z}$ plane is no longer valid, since the wave front curves backwards as discussed in the previous section. However, the instabilities remain trapped along the side wall (figure 8b and c), while the wave itself, which created the instabilities, remains stable further away. In the density field, the instabilities are recognized as interleaving layers of lighter and denser fluid associated with the roll-up of the K-H billows. The span-wise extent remains largely unchanged as the vortices leave the
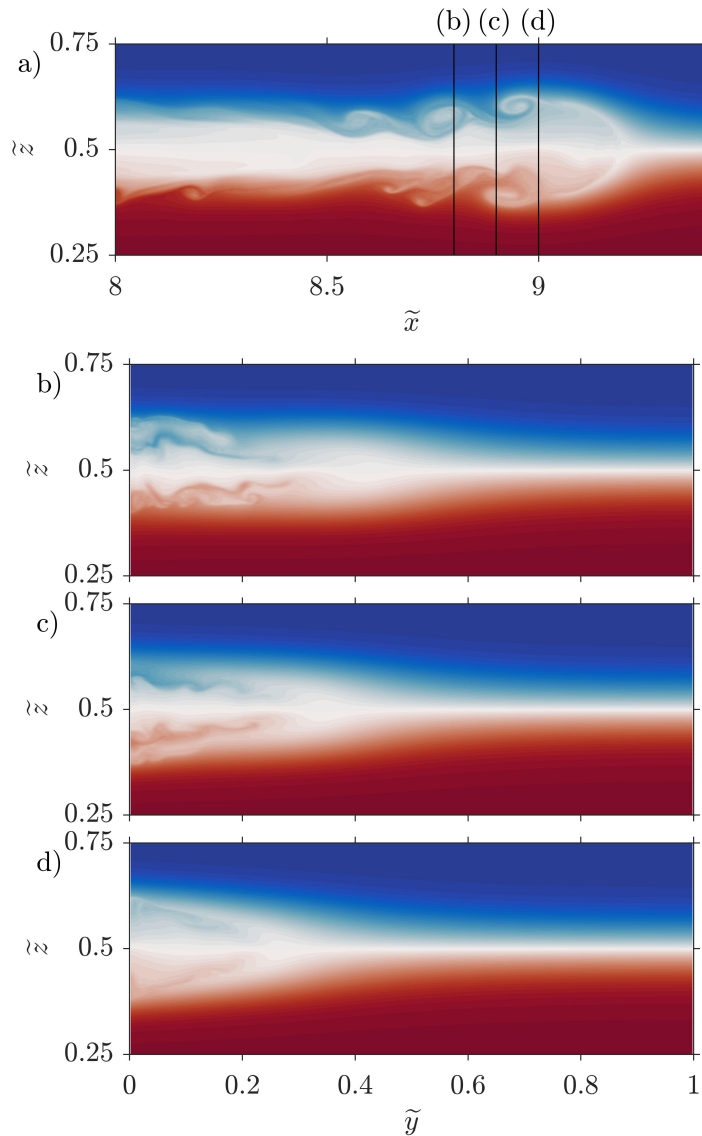
Figure 8. Density anomaly, $\widetilde{\rho}$, at $\widetilde{t} = 5.2$ ($t = 50$ s) and a) $\widetilde{y} = 0$ b) $\widetilde{x} = 8.8$ c) $\widetilde{x} = 8.9$ d) $\widetilde{x} = 9$ for case 10_1.

leading wave. This means that rotation causes mixing and turbulence to occur at a preferred location, namely on the focusing wall. Should the geometry, or environmental forcing (e.g. flow over a sill in a fjord) cause Kelvin waves to be generated at a specific location, this would indicate that one side of the channel would experience more mixing. The aforementioned fjords, as well as narrow lakes would be particularly susceptible to this.

5   We find that changes in the rotation rate (i.e. the strength of the Coriolis force) influence the intensity of the K-H billows (figure 9). Though the initial available energy is the same in all cases, the higher rotation rates lead to higher localized kinetic
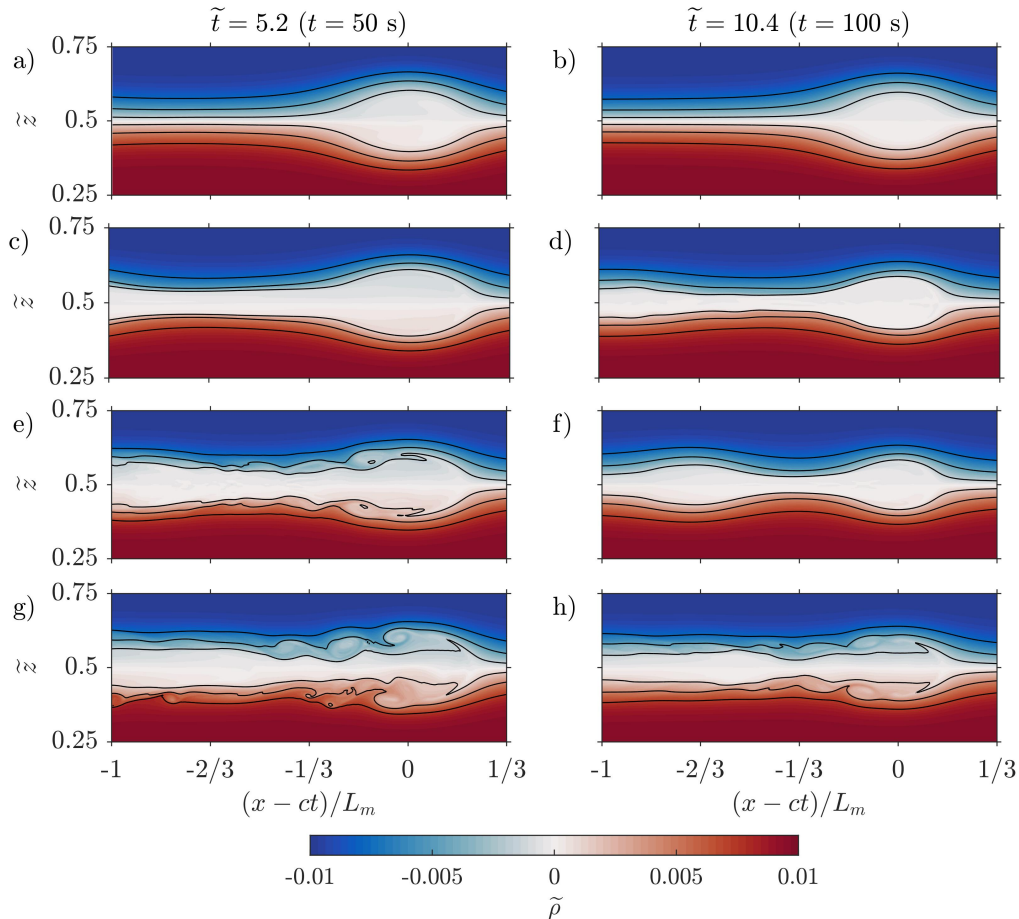
Figure 9. Density anomaly, $\widetilde{\rho}$, at $\widetilde{y} = 0$ for $f/f_0 =$ a,b) 0 c,d) 1/4 e,f) 1/2 g,h) 1. Black contours are equispaced isopycnals between $\rho(z_0 - h)$ and $\rho(z_0 + h)$. All cases have $Sc = 10$.

energy density. At early times (first column of figure 9) the amplitude of the leading waves are all comparable, but have varying levels of stability. The cases with increasing rotation are far more energetic. Fundamentally, these vortices are formed from stratified shear instabilities commonly associated with larger amplitude waves (Brandt and Shipley (2014)). This leads us to suggest that a coastally trapped wave has a lower minimum amplitude threshold for instability generation. Over time this causes
5 the wave to reduce in amplitude considerably faster than would be the case without the presence of rotation. The precise reason for the lower minimum amplitude remains an open problem, but it likely has to do with the mass and energy flux towards the focusing region discussed in the previous section.

As time progresses, the wave sheds energy and mass in the shear instabilities until reaching a critical amplitude, after which the wave continues to decay because of the lossy behaviour of the core region of large amplitude mode-2 ISWs (Deepwell
10 and Stastna (2016)). At $\widetilde{t} = 10.4$ ($t = 100$ s), only the highest rotation rate still produces shear instabilities. In comparison, the

non-rotating case is laminar and time-invariant, apart from small dissipative effects for all times. The weaker rotation rate cases do not exhibit instabilities at later times, but rather the mass from the shed vortices has formed the Kelvin wave tail. This wave is also immediately apparent from figure 3 which shows the kinetic energy within this wave directly behind the leading Kelvin wave. Over time the lower rotation rates show that this Kelvin wave tail obtains energy from the leading wave and eventually

5   overtakes it. At the highest rotation rate, the shear instability remains active for the entire simulation which makes it difficult for this wave to form.

The emergence of shear instabilities is correlated with the rotation rate. That is, a higher rotation rate is associated with an earlier shear instability. The higher rotation causes greater fluid to be directed towards the focusing wall which leads to a greater initial amplitude which creates favourable conditions for shear instabilities. Though the initial amplitude is correlated

10 with rotation rate (figure 10), the three fastest rotations result in similar wave amplitudes as the experiment continues. This leads to the interesting question of whether Kelvin waves have a stability restriction based on their amplitudes, though the form of their creation here (as a collapse of a span-wise invariant perturbation) greatly impacts the dynamics, especially with the K-H billows.
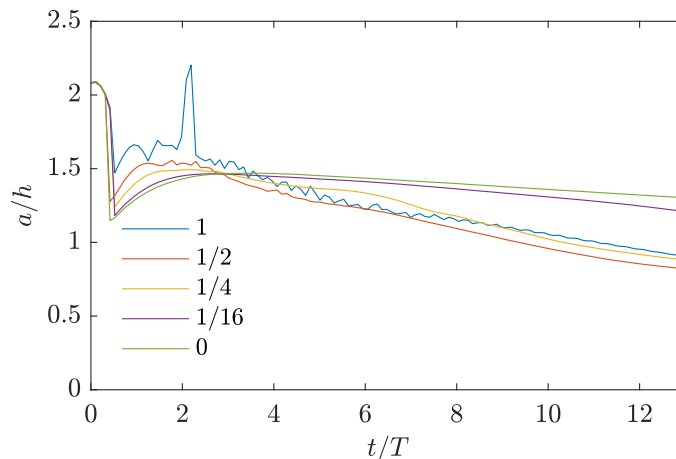
Figure 10. Wave amplitude as a function of time for different rotation rates (f/f_0 in legend). All cases have $Sc = 10$.

The wave amplitude decay rate, $a' = -\frac{T}{h}\frac{da_w}{dt}$, increases with rotation rate (table 2, and figure 10). At larger rotation rates

15 this is a result of a greater initial amplitude, while slower rates create far less K-H billows and the associated loss of mass. At $\tilde{t} = 5.2\ (t = 50\,\mathrm{s})$, the kinetic energy within the leading wave increases with rotation rate (first column of figure 11). The kinetic energy also becomes localized in space at the K-H billows. At later times, The kinetic energy has decreased most substantially in the higher rotation rates because of the shear instabilities.

Figure 12 shows the kinetic energy slices in the $\tilde{y} - \tilde{z}$ plane at the crest of the Kelvin wave (ISW in the non-rotating case).

20 The case of no rotation has an essentially span-wise invariant wave front, whereas the rotation breaks the symmetry by curving the wave front. Along the cross-section of maximum amplitude this appears as an exponential decay of the wave amplitude.
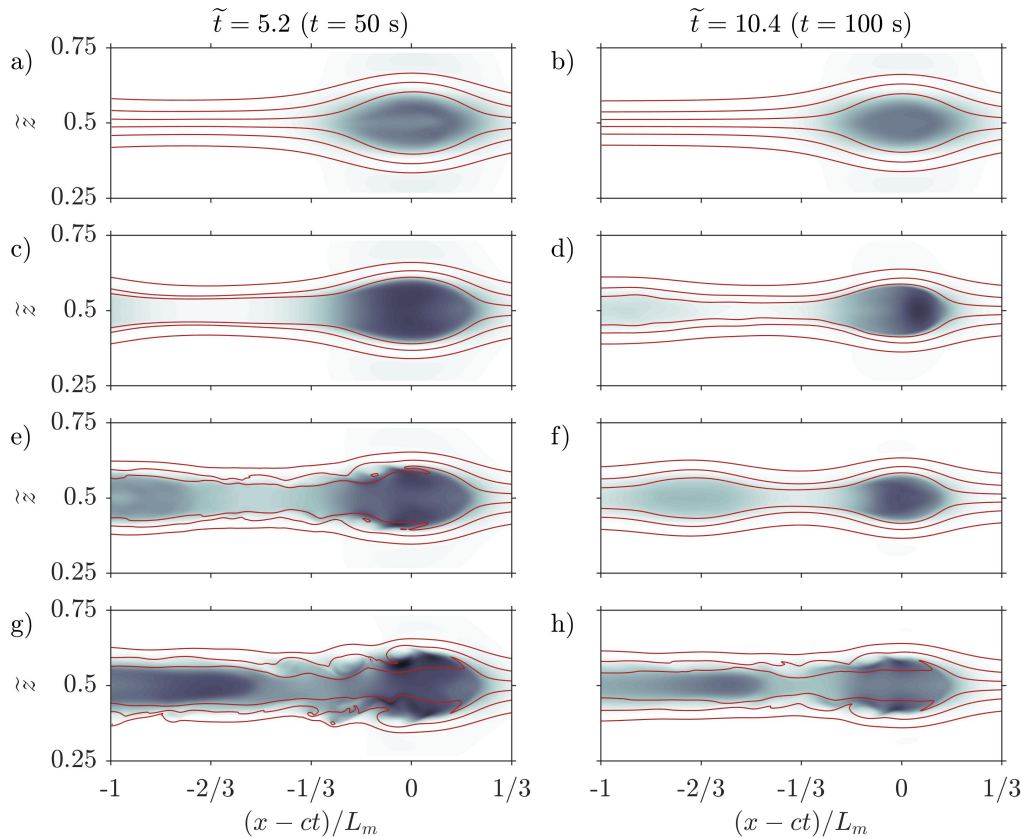
Figure 11. Kinetic energy density at at $\widetilde{y} = 0$ for $f/f_0 =$ a,b) 0 c,d) 1/2 e,f) 1. Red contours are the same as in figure 9. All cases have $Sc = 10$.

Essentially all of the kinetic energy resides within the characteristic isopycnals, $\rho(z_0 \pm h)$. Furthermore, the density overturns resulting from the instabilities are correlated with the locations of maximum KE.

Over time, due to the radiation of energy into trailing waves, the leading Kelvin wave reduces in amplitude, span-wise width, and KE. The time dependent nature of the width, and thus the exponential decay, results in an increased localization of KE along the focusing wall (seen very clearly in the second row of figure 12). This is true along the cross-section of maximum amplitude where the decaying Kelvin wave applies. In the curved portion of the leading wave, this coincides with a simple reduction of the width of the curved wavefront.

Maxworthy (1983) found that the measured Rossby radius of deformation, L_M, (that is, the distance from the wall for the amplitude to drop by a factor of e) was a factor of two smaller than the calculated Rossby radius, L_c. Only the highest rotation rate has L_M smaller than the width of the channel for us to make a comparison. Case 10_1 has the factor being close to 2.6, which is comparable. This does not appear to be the case at lower rotation rates since these cases have their amplitudes decay over the entire channel width even though the Rossby radius increase by up to a factor for 4. This could be due to the
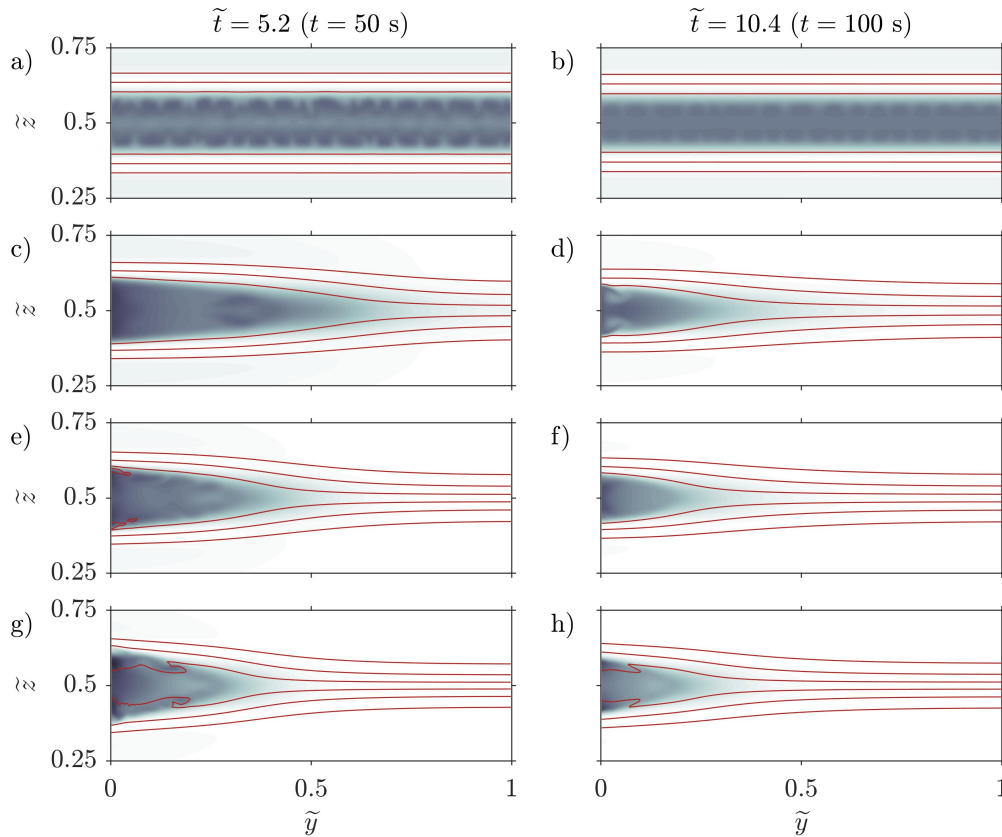
Figure 12. Kinetic energy density at the location of maximum amplitude for $f/f_0 =$ a,b) 0 c,d) 1/4 e,f) 1/2 g,h) 1. Red contours are the same as in figure 9. All cases have $Sc = 10$.

narrowness of the channel compared to the Rossby radius or more likely a difference in measurement technique. Maxworthy (1983) made their estimate based on the projection of the wave field onto the $\widetilde{y} - \widetilde{z}$ plane. This would lead to a weaker decay rate since the wave curves backwards away from the cross-section with a fixed $\tilde{x}$ at which our estimate is made. In other words the method of Maxworthy (1983) integrates in the along tank direction, while we choose a particular stream-wise location for our estimate.

4   Results: Schmidt number dependence

The shear instabilities and associated dynamics are fundamentally small scale behaviour which are damped by viscosity and smeared by diffusion, both of which are determined by the properties of the fluid, namely the molecular diffusivity and the viscosity. Experimentally, the diffusivity is fixed by the choice of stratifying solute. Physical values of a salt stratified experiment, which are typical for experiments of this type, give a Schmidt number of approximately 700. Since direct numerical

simulations at these values are unattainable due to the resolution required, we provide here a short description of the impact that various Schmidt numbers have on the results presented thus far.

For longer simulations, such as the ones conducted here, the pycnocline will diffuse causing the waves to propagate in a slightly different stratification near the end of the simulation compared to the beginning. Smaller Schmidt numbers have greater diffusion causing a greater impact (figure 13a). The $Sc = 1$ case had the pycnocline grow by 70% while the $Sc = 10$ case only grew by 10%. The background stratification at the end of the experiment is noticeably different (figure 13b).
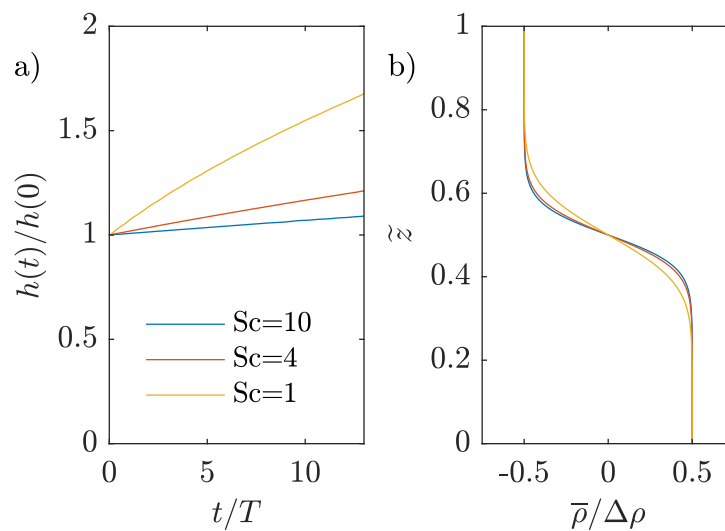
Figure 13. a) Pycnocline half-width as a function of time for different Schmidt numbers. b) The background stratification at $t/T = 12.5$ ($t = 120$ s).

We find that the wave amplitude is unaffected when compared at various Schmidt numbers. The general features characterizing the wave are thus fairly similar at $\widetilde{t} = 5.2$ ($t = 50$ s) (figure 14). The details, however, are significant enough to warrant comment. All Schmidt numbers experience the shedding of Kelvin-Helmholtz billows, but in the lowest Schmidt number case formation ceases at around $\widetilde{t} = 11.7$ ($t = 112$ s) while the other two cases never stop. Since the stratification has broadened in this case, the Richardson number has increased leaving the unstable region for shear instabilities to form.

The span-wise profile of the wave also shows the difference (right column of figure 14). The highest Schmidt number case has overturning which is not present in the lowest Schmidt number case. These features are secondary to the over-all behaviour. For example, the total kinetic energy is comparable between all cases at a given rotation rate but remains consistently weaker for lower Schmidt number. The greatest separation between the Sc=1 and Sc=10 case is 13%. As this ratio is only expected to grow as Sc increases, the difference between typical simulations of Sc=1 or Sc=7 are bound to misrepresent the smaller dynamical features of an equivalent physical experiment.
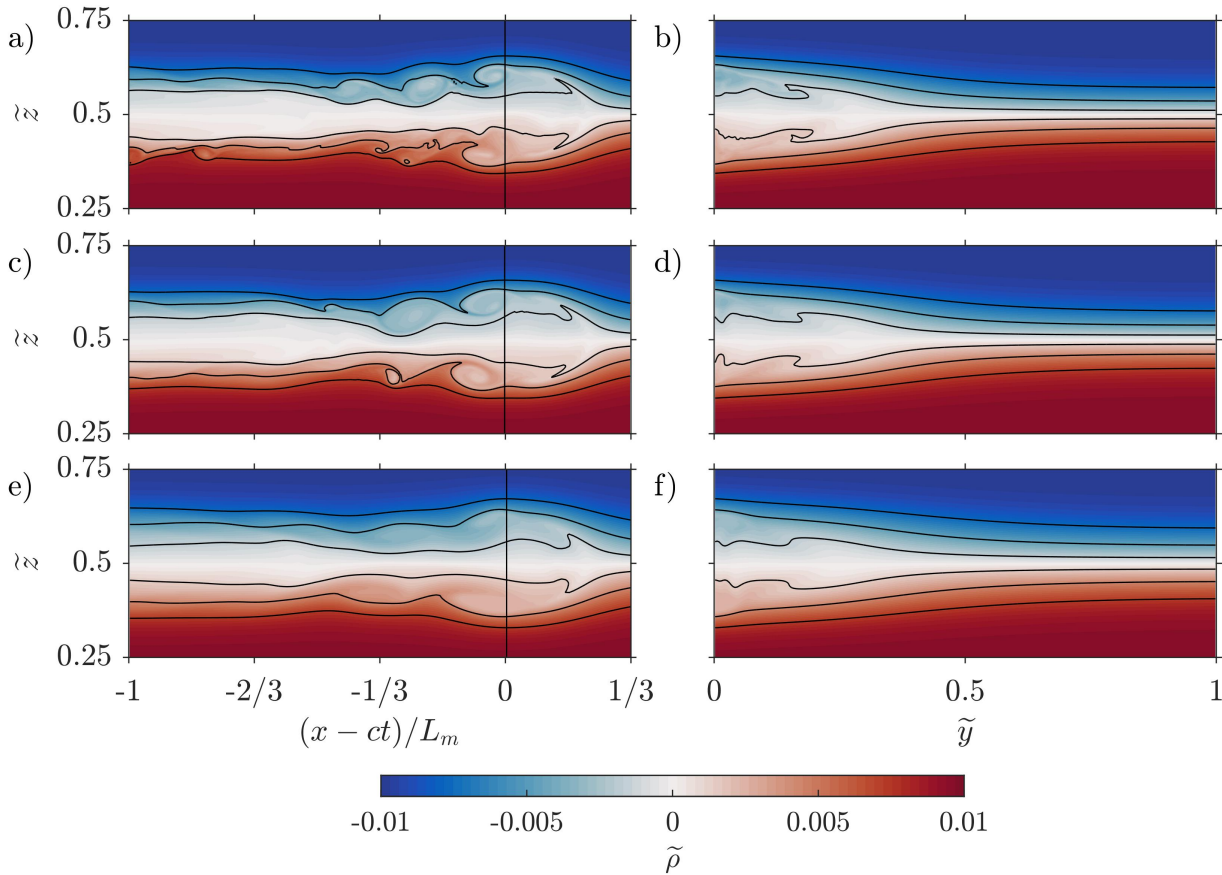
Figure 14. Density anomaly, $\widetilde{\rho}$, at $\widetilde{t} = 5.2$ ($t = 50$ s) with cross-sections at $\widetilde{y} = 0$ (first column) and at the location of maximum amplitude (second column) for Sc = a,b) 10 c,d) 4 e,f) 1. Black contours are the same as in 9. Vertical, black line denotes location of the cross-section shown in the right column. All cases have $f/f_0 = 1$.

In the $f/f_0 = 1/2$ rotation rate cases (comparison not shown) the differences are more obvious. The density field does not clearly show the Kelvin wave tail in the Sc=1 case. Rather, the wave is of such small amplitude that it is nearly indistinguishable compared to the pycnocline width. Only by looking at the vertically integrated KE does the wave appear, but is of considerably smaller magnitude. The fanning structure seen in figure 4 also goes from at least two branches in case 10_1/2 to one in case 1_1/2. This results in a different Poincaré wave field in the majority of the domain.

5   Conclusions

We have performed a series of numerical experiments of a lock–release configuration exploring the effects that rotation and side walls have on the evolution of mode-2 ISWs. When the stratification has a single pycnocline form, naturally occurring mode-2 waves are quite likely to exhibit regions of overturning and hence our configuration is ideal for exploring the combined

effects of rotation and instability. Matching with the results of Maxworthy (1983), we observe that the leading wave becomes curved by rotation and that the dominant instability takes the form of two K-H billows at the crest of the wave, above and below the pycnocline center. By modifying the rotation rate we observe that as the rate of rotation increases the instabilities become more energetic. This appears to be due to increased focusing of mass and the kinetic energy density along the focusing wall,

5 especially in the early period of adjustment after the lock is released. Since these type of shear instabilities are most commonly formed by large amplitude waves, this suggests that channel trapped waves have a lower minimum amplitude threshold for instability generation and thus will have smaller amplitude waves compared to internal solitary waves in the open ocean.

These instabilities cause the leading wave to lose energy and thus higher rotation rates result in a faster decay in wave amplitude than cases with a lower rotation rate. The increased instability generation along the side wall also serves to create

10 an asymmetry in the extent of mixing across the width of the tank. This effect could be observed in fjords or narrow lakes by making a careful comparison of mixing levels and wave amplitudes across the channel.

The high level of mass and kinetic energy along the focusing wall also resulted in the radiation of Poincaré waves, as previously described by Sánchez-Garrido and Vlasenko (2009). The Poincaré waves reflect off the opposing wall before returning to resonantly generate the secondary Kelvin wave along the focusing wall. When compared against an equivalent non-rotating

15 case we found that this generation mechanism (through resonance) at higher rotation rates was completely different from the creation of secondary ISWs in a non-rotating reference frame. We referred to this wave as the secondary Kelvin wave. In addition to this, a Kelvin wave tail formed from the remains of the focused mass and energy along the wall. During propagation, we observed that the leading Kelvin wave appeared to lose energy to the both of these Kelvin waves, each of which became more energetic and thus faster. Eventually, these trailing Kelvin waves will overtake and surpass the leading wave. The results

20 observed are fundamentally different than those seen without side walls. In the case without the side walls the leading wave energy is deposited into the trailing waves through dispersion eventually forming a wave packet. This packet has no span-wise variation. With side walls, the trailing waves are a fan of Poincaré waves that exhibit a complex interference pattern and hence have a span-wise structure. Furthermore, the energy of the leading wave is not continuously being lost to the primary trailing wave and hence this wave lives significantly longer, compared to the non-rotating case..

25 The results presented above suggest two clear avenues for future work. One avenue would focus on the rotation modified instability region. While in the above, clear evidence of transitional behaviour was presented, it is unclear to what extent a truly turbulent state was achieved. This is because trapping by the leading Kelvin wave is incomplete and turbulence may lose energy due to a spreading in space. Moreover, while the resolution of the numerical simulations was excellent for the full domain, a study that is focused on turbulent transition could optimize the domain and stratification parameters. For example, the domain

30 could be shortened and the initial perturbation increased in size to increase the wave amplitude. A second possible avenue for future work would explore the effect of the span-wise extent. Figure 15 of Sánchez-Garrido and Vlasenko (2009) suggests that for wider domains, mode-1 Kelvin waves yield Poincaré wave trains whose focusing yields Mach stems on the far wall. We did not observe this phenomenon in our simulations, but it is possible that our span-wise extent was simply not large enough to achieve this. Of course, an experimental realization of our simulations would provide both a test of our results, and suggestions

35 for future numerical studies that are most relevant to the experimentalist.

Competing interests. No competing interests are known.

Acknowledgements. Time dependent simulations were completed on the high-performance computer cluster Shared Hierarchical Academic Research Computing Network (SHARCNET, www.sharcnet.ca). DD and AC were supported by an Ontario Graduate Scholarships while MS was supported by an NSERC Discovery Grant RGPIN-311844-37157.

References

Benjamin, T. B.: Internal waves of permanent form in fluids of great depth, J. Fluid Mech., 29, 559, https://doi.org/10.1017/s002211206700103x, http://dx.doi.org/10.1017/S002211206700103X, 1967.

Bourgault, D. and Kelley, D. E.: Wave-induced boundary mixing in a partially mixed estuary, Journal of Marine Research, 61, 553–576, https://doi.org/10.1357/002224003771815954, https://doi.org/10.1357%2F002224003771815954, 2003.

Brandt, A. and Shipley, K. R.: Laboratory experiments on mass transport by large amplitude mode-2 internal solitary waves, Physics of Fluids, 26, 046 601, https://doi.org/10.1063/1.4869101, http://dx.doi.org/10.1063/1.4869101, 2014.

Coutino, A. and Stastna, M.: The fully nonlinear stratified geostrophic adjustment problem, Nonlinear Processes in Geophysics, 24, 61, https://doi.org/10.5194/npg-24-61-2017, https://doi.org/10.5194/npg-24-61-2017, 2017.

Deepwell, D. and Stastna, M.: Mass transport by mode-2 internal solitary-like waves, Physics of Fluids, 28, 056 606, https://doi.org/10.1063/1.4948544, http://dx.doi.org/10.1063/1.4948544, 2016.

Farmer, D., Li, Q., and Park, J.-H.: Internal wave observations in the South China Sea: The role of rotation and non-linearity, Atmosphere-Ocean, 47, 267–280, https://doi.org/10.3137/oc313.2009, https://doi.org/10.3137/oc313.2009, 2009.

Fedorov, A. V. and Melville, W. K.: Propagation and breaking of nonlinear Kelvin waves, Journal of physical oceanography, 25, 2518–2531, https://doi.org/10.1175/1520-0485(1995)025<2518:pabonk>2.0.co;2, https://doi.org/10.1175/1520-0485(1995)025%3C2518:PABONK%3E2.0.CO;2, 1995.

Grimshaw, R.: Evolution equations for weakly nonlinear, long internal waves in a rotating fluid, Studies in Applied Mathematics, 73, 1–33, https://doi.org/10.1002/sapm19857311, http://dx.doi.org/10.1002/sapm19857311, 1985.

Grimshaw, R. H. J., Helfrich, K. R., and Johnson, E. R.: Experimental study of the effect of rotation on nonlinear internal waves, Physics of Fluids, 25, 056 602, https://doi.org/10.1063/1.4805092, https://doi.org/10.1063/1.4805092, 2013.

Hosegood, P. and van Haren, H.: Near-bed solibores over the continental slope in the Faeroe-Shetland Channel, Deep Sea Research Part II: Topical Studies in Oceanography, 51, 2943–2971, https://doi.org/10.1016/j.dsr2.2004.09.016, http://www.sciencedirect.com/science/article/pii/S0967064504002012, small and mesoscale processes and their impact on the large scale, 2004.

Katsis, C. and Akylas, T. R.: Solitary internal waves in a rotating channel: A numerical study, Physics of Fluids, 30, 297–301, https://doi.org/10.1063/1.866377, https://doi.org/10.1063/1.866377, 1987.

Klymak, J. M. and Gregg, M. C.: Three-dimensional nature of flow near a sill, Journal of Geophysical Research: Oceans, 106, 22 295–22 311, https://doi.org/10.1029/2001jc000933, http://dx.doi.org/10.1029/2001JC000933, 2001.

Kundu, P. K., Cohen, I. M., and Dowling, D. R.: Fluid Mechanics, Academic Press, 5th edn., 2012.

Kuo, A. C. and Polvani, L. M.: Time-dependent fully nonlinear geostrophic adjustment, Journal of Physical Oceanography, 27, 1614–1634, https://doi.org/10.1175/1520-0485(1997)027<1614:tdfnga>2.0.co;2, https://doi.org/10.1175/1520-0485(1997)027%3C1614:TDFNGA%3E2.0.CO;2, 1997.

Lamb, K. G.: On boundary-layer separation and internal wave generation at the Knight Inlet sill, Proceedings of the Royal Society A: Mathematical, Physical and Engineering Sciences, 460, 2305–2337, https://doi.org/10.1098/rspa.2003.1276, https://doi.org/10.1098/rspa.2003.1276, 2004.

Maxworthy, T.: Experiments on solitary internal Kelvin waves, Journal of Fluid Mechanics, 129, 365–383, https://doi.org/10.1017/s0022112083000816, http://www.journals.cambridge.org/abstract_S0022112083000816, 1983.

Mertz, G. and Gratton, Y.: Topographic Waves and Topographically Induced Motions in the St Lawrence Estuary, pp. 94–108, Springer-Verlag, https://doi.org/10.1002/9781118663783.ch5, http://dx.doi.org/10.1002/9781118663783.ch5, 2013.

Renouard, D. P., D'Hières, G. C., and Zhang, X.: An experimental study of strongly nonlinear waves in a rotating system, Journal of Fluid Mechanics, 177, 381–394, https://doi.org/10.1017/s0022112087001009, http://www.nonlin-processes-geophys.net/16/587/2009/%25, 1987.

5 Salloum, M., Knio, O. M., and Brandt, A.: Numerical simulation of mass transport in internal solitary waves, Physics of Fluids, 24, 016 602, https://doi.org/10.1063/1.3676771, https://doi.org/10.1063%2F1.3676771, 2012.

Sánchez-Garrido, J. C. and Vlasenko, V.: Long-term evolution of strongly nonlinear internal solitary waves in a rotating channel, Nonlinear Processes in Geophysics, 16, 587–598, https://doi.org/10.5194/npg-16-587-2009, https://www.nonlin-processes-geophys.net/16/587/2009/, 2009.

10 Scotti, A. and Pineda, J.: Observation of very large and steep internal waves of elevation near the Massachusetts coast, Geophysical Research Letters, 31, L22 307, https://doi.org/10.1029/2004gl021052, http://dx.doi.org/10.1029/2004GL021052, 2004.

Shroyer, E. L., Moum, J. N., and Nash, J. D.: Mode 2 waves on the continental shelf: Ephemeral components of the nonlinear internal wavefield, Journal of Geophysical Research, 115, https://doi.org/10.1029/2009jc005605, https://doi.org/10.1029%2F2009jc005605, c07001, 2010.

15 Subich, C. J., Lamb, K. G., and Stastna, M.: Simulation of the Navier-Stokes equations in three dimensions with a spectral collocation method, Int. J. Num. Meth. Fluids, 73, 103–129, https://doi.org/10.1002/fld.3788, http://dx.doi.org/10.1002/fld.3788, 2013.

Terez, D. E. and Knio, O. M.: Numerical simulations of large-amplitude internal solitary waves, Journal of Fluid Mechanics, 362, 53–82, https://doi.org/10.1017/S0022112098008799, http://journals.cambridge.org/article_S0022112098008799, 1998.

Ulloa, H. N., de la Fuente, A., and Niño, Y.: An experimental study of the free evolution of rotating, nonlinear internal gravity waves in a two-
20 layer stratified fluid, Journal of Fluid Mechanics, 742, 308–339, https://doi.org/10.1017/jfm.2014.10, https://doi.org/10.1017/jfm.2014.10, 2014.

Ulloa, H. N., Winters, K. B., de la Fuente, A., and Niño, Y.: Degeneration of internal Kelvin waves in a continuous two-layer stratification, Journal of Fluid Mechanics, 777, 68–96, https://doi.org/10.1017/jfm.2015.311, https://doi.org/10.1017/jfm.2015.311, 2015.